Iran University of Science and Technology

International Journal of

Railway Research

ISSN: 2423-3838

Fast Hybrid Circuit Breaker for Medium-Voltage DC and AC Railway Power Supply Networks: A Simulation-Based Study

Ahmad Olyaei [1], Rozbeh Asad [1*]

[1] School of Railway Engineering, Iran University of Science and Technology, Tehran, Iran

ARTICLE INFO

Article history:

Received: 20.04.2025

Accepted: 20.05.2025

Published: 18.09.2025

Keywords:

High-Speed Circuit Breaker

Hybrid Circuit Breaker

CCDC Topology

LCS Topology

A B S T R A C T

This paper investigates the performance of a medium-voltage hybrid circuit breaker designed for the protection of electrical power supply networks in railway transportation systems. Two primary topologies, namely LCS (Load Commutation Switch) and CCDC (Current Commutation Drive Circuit), are analyzed for AC and DC networks, respectively. Leveraging recent advancements in semiconductor technology and power electronics, novel approaches are introduced to enhance efficiency and reduce fault-clearing times. The performance of hybrid circuit breakers in medium-voltage AC and DC networks is evaluated using LTspice and PSpice simulation environments. The results demonstrate that the proposed hybrid circuit breaker achieves efficient fault protection with fault-clearing times of less than 10 milliseconds, outperforming conventional systems. Given the critical importance of protection in railway electrical power supply networks, this study proposes enhancements in protective characteristics, particularly in fault-clearing speed, through the application of hybrid circuit breakers.

1. Introduction

Electrical networks in railway transportation systems, particularly in metro and electrified railway lines, require advanced protection mechanisms to ensure safety and reliability. The growing demand for sustainable transportation and the development of electrified infrastructure have introduced challenges such as fault management and reduced protection response times.

Traditional electromechanical circuit breakers, while effective in the past, exhibit limitations in modern medium-voltage (5–33 kV) AC and DC power supply networks, including slow switching times (25–75 ms). Hybrid circuit breakers (HCBs), combining mechanical switches and solid-state switches, offer an innovative solution with high speed, low losses, and extended operational life.

Electrical protection has been a critical concern since the development of electrical grids in the 19th century. Early mechanical circuit breakers were suitable for AC networks but exhibited limited performance in DC networks, where the current does not naturally cross zero [1]. With the advent of DC microgrids and high-voltage DC (HVDC) systems, the need for faster circuit breakers became evident. Solid-state circuit breakers (SSCBs), utilizing semiconductors such as SiC MOSFETs and

*Corresponding author

Email address: asad@iust.ac.ir

Insulated Gate Bipolar Transistors (IGBTs), reduced fault-clearing times to microseconds but introduced challenges such as high conduction losses and elevated costs [2]. Hybrid circuit breakers (HCBs), combining mechanical and solid-state switches, mitigate these issues. Studies indicate that HCBs perform effectively in medium- and high-voltage applications (up to 500 kV) [3]. In the context of railway transportation, research has primarily focused on power supply systems, with limited exploration of HCB applications [20]. In this study addresses this gap by leveraging CCDC topology for DC networks and LCS topology for AC networks, incorporating advanced semiconductor technologies. Recent advancements in wide-bandgap (WBG) materials, such as SiC, have improved system efficiency and reduced losses [4]. Building on this foundation, this research proposes a novel HCB design for railway power supply networks.

The current study examines the design of a hybrid circuit breaker tailored for railway power supply network protection, aiming to minimize fault-clearing time and enhance fault-handling efficiency. Software simulations were employed to evaluate the proposed design's performance and demonstrates its superiority over traditional circuit breakers. This research focuses on the practical application of hybrid circuit breakers in railway transportation and proposes solutions to improve protection in medium-voltage networks.

2. Approach

2.1 Structure of Hybrid Circuit Breakers

Figure 1 illustrates the general structure of a hybrid circuit breaker, comprising four main components: a mechanical switch, solid-state switches, an auxiliary commutation circuit (ACC), and energy absorption devices [6]. In this circuit diagram, metal oxide varistors (MOVs) are considered as the primary energy absorption devices due to their widespread use. Mechanical switches are essential in HCBs, conducting nominal current with very low resistance (often less than 1 mΩ), resulting in negligible power losses in the ON state [7]. However, the slow movement of mechanical contacts can significantly delay fault interruption, necessitating ultra-fast actuation mechanisms. Two types of HCBs are identified: arc-capable circuit breakers and non-arc-capable isolators [8].

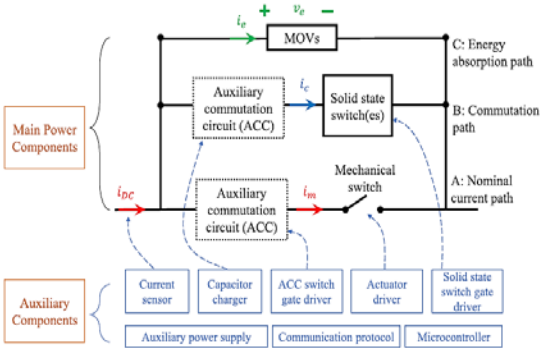

Figure 1. Analytical structure of a hybrid circuit breaker [6].

Arc-capable mechanical breakers, while eliminating the need for an ACC, have limitations, such as arcing durations exceeding several milliseconds, making them more suitable for low-voltage DC (LVDC) applications where arc management is feasible [9]. However, in LVDC systems, HCBs typically lag behind SSCBs in terms of operational speed and economic durability [2].

Non-arc mechanical breakers excel in rapid contact separation (often within milliseconds) compared to arc-capable breakers [10]. This advantage, however, requires an ACC to manage fault currents [11]. Such configurations are prevalent in medium-voltage DC (MVDC) and HVDC systems, where arcing poses significant challenges. The ACC is a unique component in HCBs, absent in mechanical or solid-state switches alone. While not essential for topologies with natural arc commutation or arc-capable mechanical breakers, an ACC is critical for ultra-fast breakers aiming to reduce interruption times below milliseconds. The ACC facilitates current transfer from the mechanical switch branch to the solid-state switch branch during fault development [6]. Once a fault is detected, the ACC is activated to mitigate fault current escalation. Solid-state switches in HCBs manage the transferred fault current and initiate interruption by diverting it to MOVs. These switches transition from conducting to non-conducting states in microseconds, replacing the traditional arcing mechanism of conventional breakers. Finally, MOVs act as voltage-clamping and energy-dissipation devices [11, 12], effectively reducing fault currents to zero, analogous to the arc interruption in traditional breakers.

2.1.1. Operating Mechanism of Hybrid Circuit Breakers

The operation of an HCB can be described in a five-stage process: (1) normal operation, (2) fault detection, (3) current commutation, (4) current holding, and (5) energy absorption. The circuit configuration for each stage is depicted in Figure 2, with corresponding current and voltage waveforms shown in Figure 3 [13].

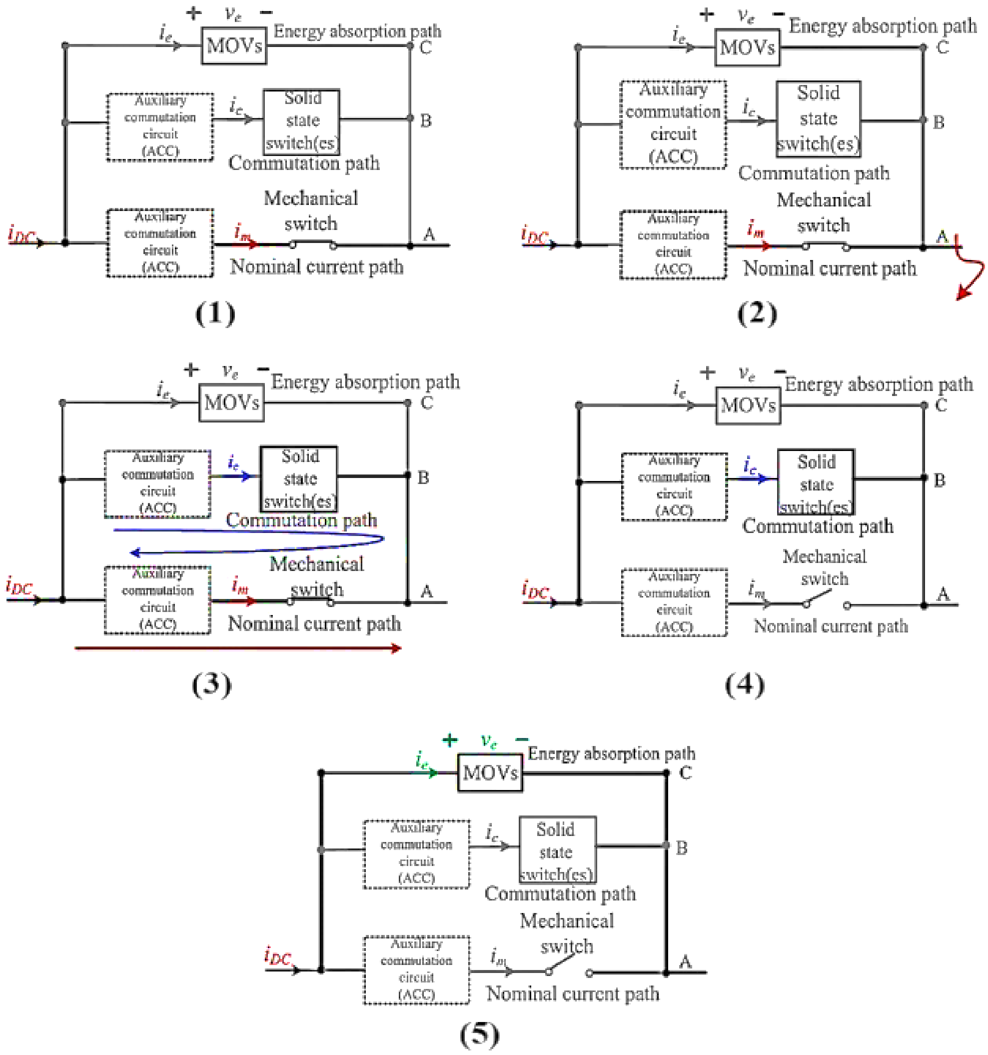

Figure 2. Circuit configurations during HCB operation: (1) normal state, (2) fault detection, (3) current commutation, (4) current holding, (5) energy absorption [6].

Normal Operation: Figure 2(1) illustrates the circuit's current path during normal operation, with corresponding current and voltage waveforms in Figure 3 (Region 1). The main current flows through the primary path with a nominal current I0, and the mechanical switch current (shown as a red dashed line) equals the main current.

Fault Detection (t_0–t_1): Figure 2(2) shows the main current path during fault detection, with waveforms in Figure 3 (Region 2). A fault occurs at t0, causing the main current to increase at a specific rate until it reaches the threshold value. This current rate is influenced by factors such as the source and line inductance [14, 15].

Commutation Process (t_1–t_2): Figure 2(3) depicts the main current during commutation, with current and voltage waveforms in Figure 3 (Region 3). Upon reaching t1, the commutation process commences, redirecting the nominal current (i.e., fault current) to the commutation path via the ACC. Consequently, the nominal current im decreases, while the commutation path current ic increases. The process concludes at t_2, at which point the fault current is fully diverted to the commutation path, resulting in i_m reaching zero. As a result, i_c equals the fault current, indicating the completion of the current commutation process.

Current Holding (t_2–t_4): Figure 2(4) shows the main current during the holding phase, with current and voltage waveforms in Figure 3 (Region 4). The fault current i_b increases until t_3, then transfers to the energy absorption path, with the MOV voltage rising. The mechanical switch opens during this period, and by t_4, the fault current flows solely through the MOVs.

Energy Absorption (t_4–t_5): Figure 2(5) illustrates the main current during energy absorption, with current and voltage waveforms in Figure 3 (Region 5). By t_5, the fault current is fully extinguished by the MOVs, and the voltage across the MOVs equals the source voltage. If an isolating switch is used in series with the HCB, it opens after fault clearance, resulting in zero voltage across the MOVs.

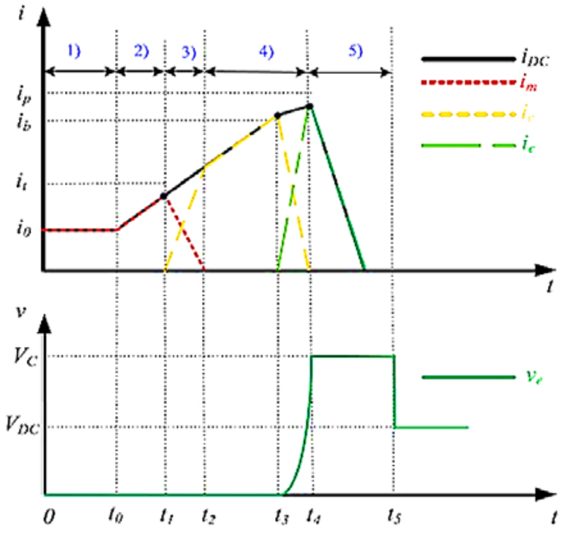

Figure 3. Current and voltage characteristics of an HCB during fault operation [6].

Figure 3 provides a fundamental representation of the operational sequence of HCBs with sequential timing. However, it is noteworthy that the actual waveform may exhibit slight variations depending on the specific topology employed. For instance, in topologies utilizing an LC circuit as the ACC, the fault current during t_1 and t_2 may display an exponential decay as part of the resonant waveform. Due to the necessity for rapid commutation, the commutation time can be significantly shorter than the resonant cycle, allowing the current decay to be approximated as a linear function rather than an exponential one [16].

2.1.2. Commutation Methods in HCBs

As shown in Figure 4, three primary commutation mechanisms are summarized for various HCB topologies: arc-based commutation, zero-voltage commutation, and zero-current commutation [6]. The latter two are classified as controlled commutation with minimal or no arcing.

*Corresponding author
Email address: asad@iust.ac.ir

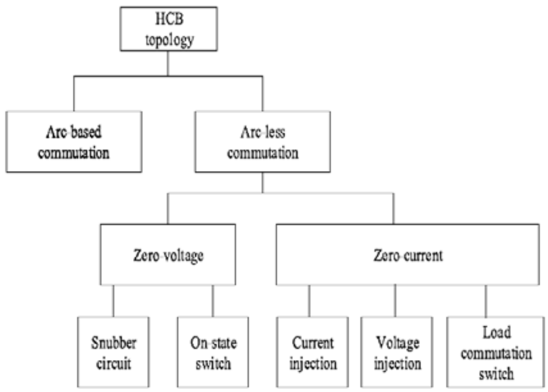

Figure 4. Main commutation methods in HCBs

Arc-Based Commutation: This method uses a simple structure with a mechanical switch in the main path and parallel solid-state switches without an ACC. Upon fault detection, the mechanical switch opens under fault conditions, forming an arc.

Zero-Voltage Commutation: This approach aims to limit the voltage across the mechanical switch during opening. A snubber circuit, often an RCD configuration, is used to manage energy stored in capacitors during re-closing [17].

Zero-Current Commutation: As shown in Figure 5, this method creates a zero-current condition, enabling the mechanical switch to open with minimal or no arcing. It is divided into three strategies: current injection, voltage injection, and load-switching commutation.

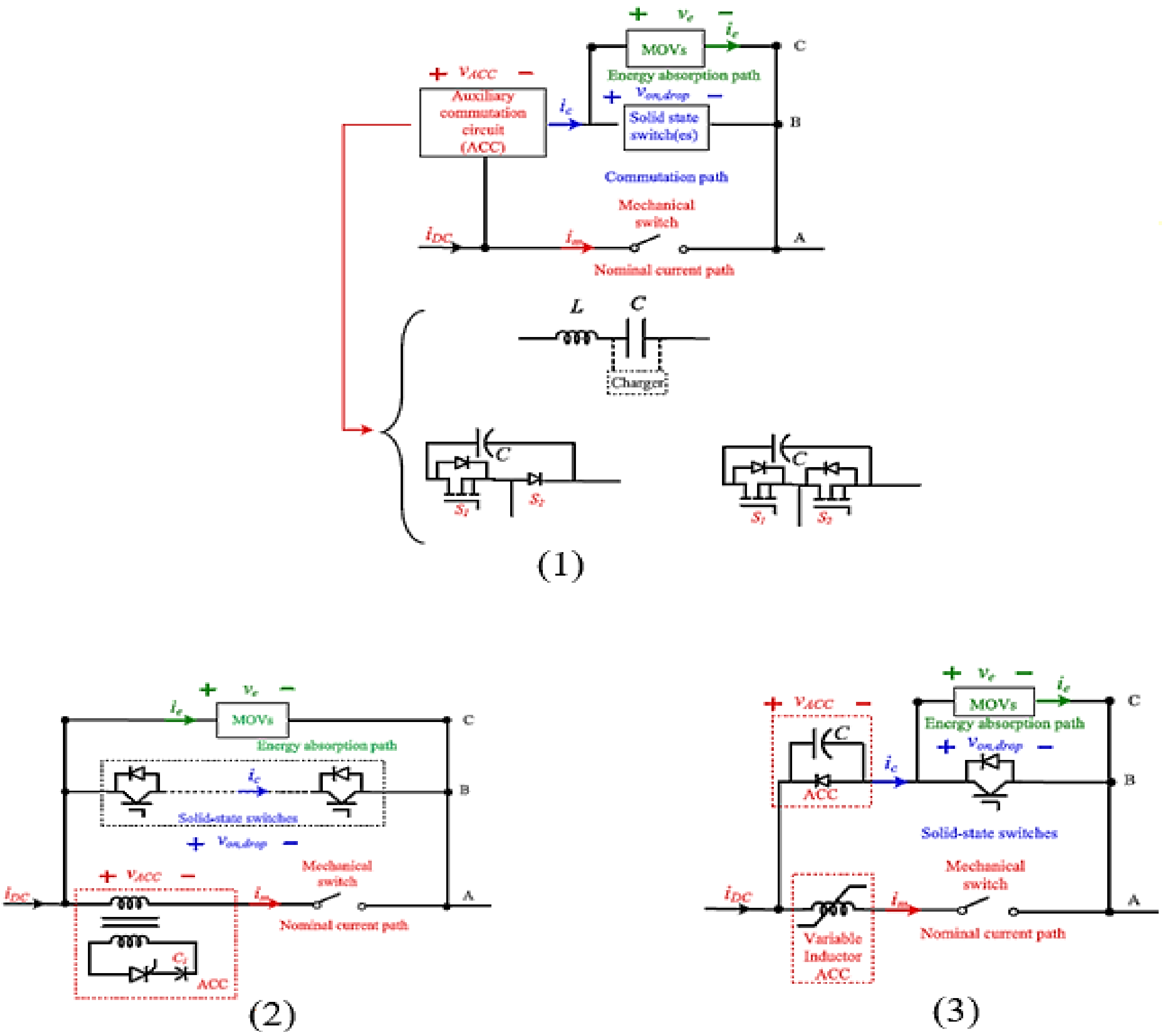

Figure 5. Classification of HCB topologies based on ACC placement [6].

The injection of current from the auxiliary commutation circuit is utilized to introduce a counteracting current opposite to the fault current, resulting in the neutralization of the fault current toward zero. Upon achieving this state, the mechanical switch can be disengaged under zero-current conditions. Based on the relative position of the auxiliary commutation circuit, HCBs can be further classified into three subgroups, as illustrated in Figure 5. In Figure 5(1), the ACC is positioned within the commutation path; in Figure 5(2), the ACC is aligned along the nominal current path; and in Figure 5(3), configurations are depicted with the ACC present in both the commutation and nominal current paths. The load commutation switch or commutation circuit consists of one or a set of solid-state semiconductors, with various proposed structures. These include configurations such as a low-voltage, high-current switch, as shown in Figure 6, structure d, or designs incorporating a full-bridge arrangement, as observed in structures e and f.

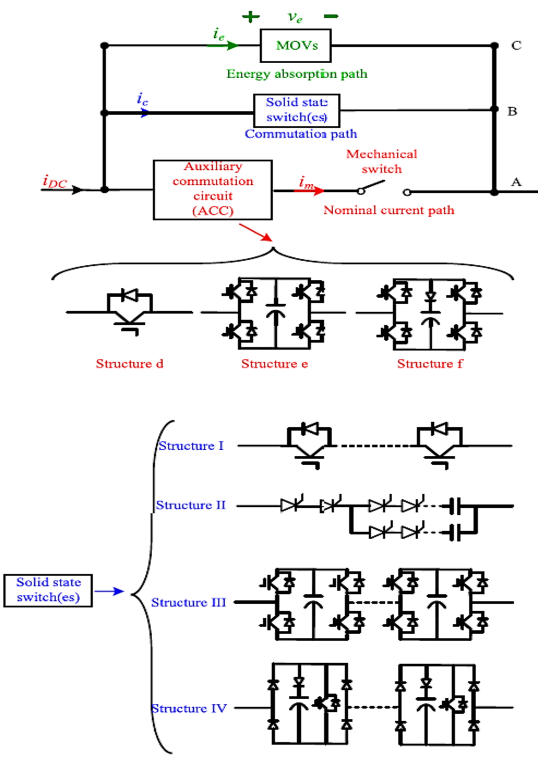

Figure 6. Configuration of Commutation Circuit Switches or ACC in Hybrid Circuit Breakers [6].

Solid-state switches can also adopt diverse configurations, ranging from series or parallel arrangements in structure 1, to Gate Turn-Off (GTO) thyristor-based designs in structure 2, or full-bridge configurations integrating fully controllable IGBTs and diodes in structures 3 and 4, respectively. These configurations are particularly applicable in operational HVDC projects [18],[19].

A comparison of commutation strategies is provided in Table 1.

Table 1. Comparison of Commutation Mechanisms

Arc-Based Commutation		
Advantages	**Disadvantages**	
Simple topology, easy implementation	Arc issues, reduced mechanical switch reliability	
Arc-less Commutation		
Topology	**Advantages**	**Disadvantages**
Zero-Voltage Commutation	Minimal arcing, no pre-charged circuit	Requires snubber design, fully controllable devices
Zero-Current Commutation (Current Injection)	Fast commutation, minimal arcing	Additional control for zero-current, often requires pre-charged circuit
Zero-Current Commutation (Voltage Injection)	Similar to current injection	Requires full DC voltage
Zero-Current Commutation (Load Switching)	Fast commutation, maintains zero current	Power losses

3. Methodology

In this study, a hybrid circuit breaker is proposed, specifically designed to align with the operational requirements of the target electrical network, which includes power supply systems for electric vehicles such as trains, trams, or electric buses. The breaker incorporates a CCDC topology for DC applications and a LCS topology for AC protection. The methodology does not

*Corresponding author
Email address: asad@iust.ac.ir

prioritize the control of the breaker under fault conditions; rather, it considers a scenario where a train is operating at maximum current consumption midway along its route. As illustrated in Figure 7, the strategic placement of the hybrid circuit breaker is defined. However, the fault location, influenced by varying short-circuit impedances, may impact performance. The primary focus remains on the breaker's interruption capability and operational efficiency, as rapid fault current interruption is deemed critical under any fault scenario, irrespective of the train or bus's position. Control commands are executed within a software environment and transmitted to the associated switch and power semiconductors. Due to the distinct topologies employed by the proposed breaker, two separate simulation groups are established. In the initial phase, the breaker is designed and simulated for a DC network based on the proposed model, while for an AC network, the model is developed and simulated in accordance with the specific network parameters. The rationale for adopting these topologies in the respective simulations is twofold. For the DC hybrid breaker, the CCDC topology, which facilitates current injection into the mechanical switch branch, is selected due to its relatively low control and circuit complexity. This characteristic is advantageous for protective switches deployed in operational railway power supply networks, as it substantially reduces maintenance and operational costs. Additionally, the mechanical switch in the hybrid breaker can utilize either conventional mechanisms or fast-acting actuators, such as Thomson or piezoelectric types. The proposed system incorporates a fast-acting Thomson actuator, which enables the shared use of battery resources within the charged capacitor circuit. For the AC network's hybrid breaker, this configuration significantly reduces interruption time and simplifies the series commutation circuit within the mechanical switch branch.

3.1. DC Power Supply Network

Depending on the research objectives, voltage levels ranging from 7.5 to 24 kV are investigated for application in MVDC power supply networks. As depicted in Figure 7, the MVDC power supply network combines the advantages of both LVDC and MVAC networks [20]. The performance of the HCB when utilized for protecting DC feeders in railway substations has been simulated using PSpice software. To further elucidate the model concept and circuit parameters, a schematic based on a single-line power supply network structure is presented in Figure 7.

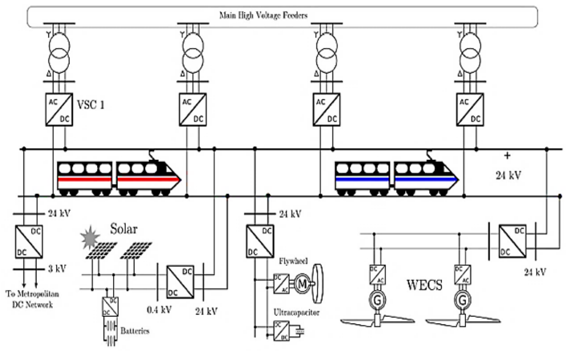

Figure 7. Multi-terminal VSC network with a 24 kV DC voltage level [29].

The detailed parameters of the power supply circuit are provided in Table 2.

Table 2. DC Network Parameters

Parameter	Symbol	Value	Unit
Source Parameters			
Source Voltage	V_S	24	kV-DC
Equivalent Resistance	R_S	0.6	Ω
Equivalent Inductance	L_S	1.2	mH
Line Parameters			
Equivalent Resistance	R_L	9	Ω
Equivalent Inductance	L_L	21.8	mH
Load Parameters			
Equivalent Resistance	R_O	135	Ω
Equivalent Inductance	L_O	0.6	H

Note that parameter values may vary slightly, with efforts made to align them with realistic conditions for VSC sources, distribution lines, and loads.

3.2. Electrical Model of the Mechanical Switch in PSpice

The realistic model of the DC mechanical switch is shown in Figure 8. It integrates a Thomson actuator model and a switch performance model, designed in LTspice and incorporated into PSpice.

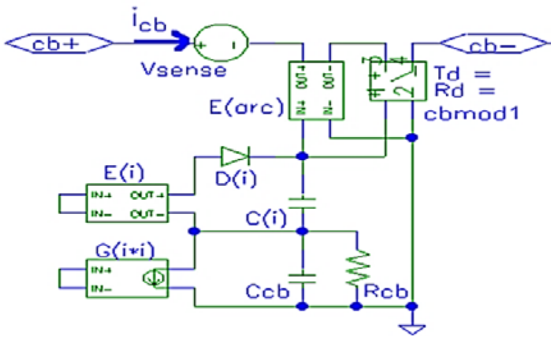

Figure 8. Detailed model of the mechanical switch in PSpice [30].

The magnetic characteristics of the switch are defined in the E(i) block, incorporating Thomson actuator parameters such as speed, force, contact distance, and coil properties (Figure 9). The switch performance model, including arc parameters, voltage drop, ON/OFF resistance, hysteresis, and transition time, is added to the E(arc) block.

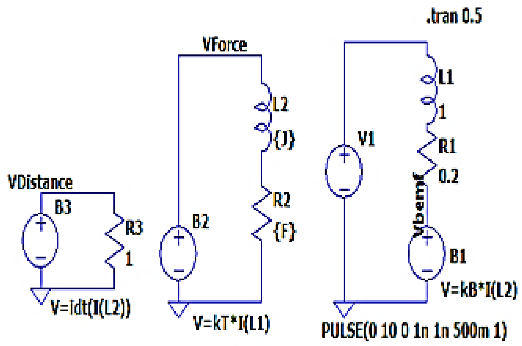

Figure 9. Proposed Thomson actuator model in LTspice.

Due to the complexity of Thomson actuator models, they are not readily available in standard PSpice or LTspice libraries and are integrated as a switch component in PSpice.

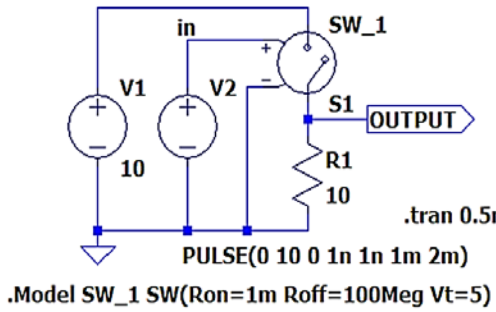

Figure 10. Mechanical switch performance model in LTspice.

3.3. Electrical Model of MOV

As shown in Figure 11, all semiconductors in the MCB branch turn off simultaneously, subjecting all MOVs to the same post-fault transient. Thus, MOVs and MCB devices can have equal blocking voltages. In progressive switching, MOVs across early-opening solid-state switches carry current longer, leading to uneven thermal stress and potential MOV failure, reducing breaker reliability. As depicted in Figure 11, MOV1 carries significantly higher current compared to the other MOVs.

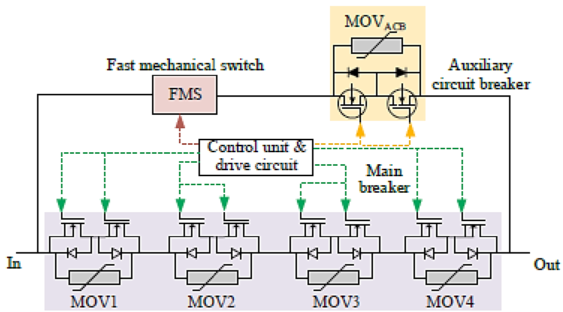

Figure 11. Schematic of the Hybrid Circuit Breaker [31].

The fault current for a DC hybrid breaker is estimated using Equations 1 and 2:

$$i(t) = \left(\frac{V_s}{R_{eq1}} - \frac{V_s}{R_{eq2}}\right) e^{-\frac{R_{eq2}}{Leq}(t - t_{fault})} + \frac{V_s}{R_{eq2}} \quad (1)$$

$$i_{MOV}(t) = \left(i(t_j) - \frac{\Delta V_j}{R_{eq}}\right) e^{-\frac{R_{eq}}{Leq}(t - t_j)} + \frac{\Delta V_j}{R_{eq}} \quad (2)$$

The energy dissipated in MOVs is approximated by Equation 3:

$$E_{MOV}(j) = \int_{0}^{t_{clear}} i_{MOV}(t) V_{MOV}(j)\, dt \qquad (3)$$

From Equation (1-3) and with reference to Figure 11, it is evident that if the MOVs in each stage have the same voltage clamping rating, they will absorb different amounts of energy across various stages. This results in uneven thermal stress on the MOVs, which can lead to performance failure of the MOVs, thereby reducing the lifespan and reliability of the circuit breaker.

Given that the maximum voltage across the MOV is significantly determined by the duration of the current surge it must absorb, a transient model for the MOV is proposed. This effect is not incorporated in the Simulink MOV model or the PSpice library and is illustrated in Figure 12. The varistors A_0 and A_1 can be modeled using the configuration shown in the Figure 12. Subsequently, the values of A_0 and A_1 are adjusted to achieve discharge voltages corresponding to the oscillatory switching discharge currents [24]. Additionally, L_1 can be tuned to align with the datasheet discharge voltage for discharge currents ranging from 8 to 20 seconds, ensuring a high degree of conformity [25].

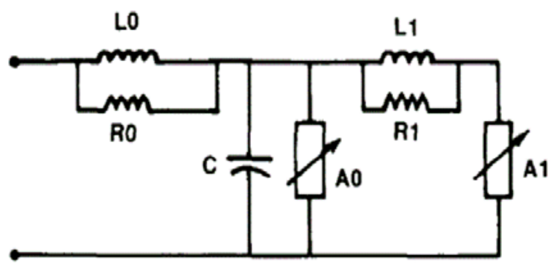

Figure 12. Proposed MOV model

3.4. CCDC Topology

The CCDC topology, utilizing a coupled inductor as an ACC, is simulated as shown in Figure 13(1). The CCDC is a critical component for ensuring successful commutation in a high- and medium-voltage HCB [22], [23].

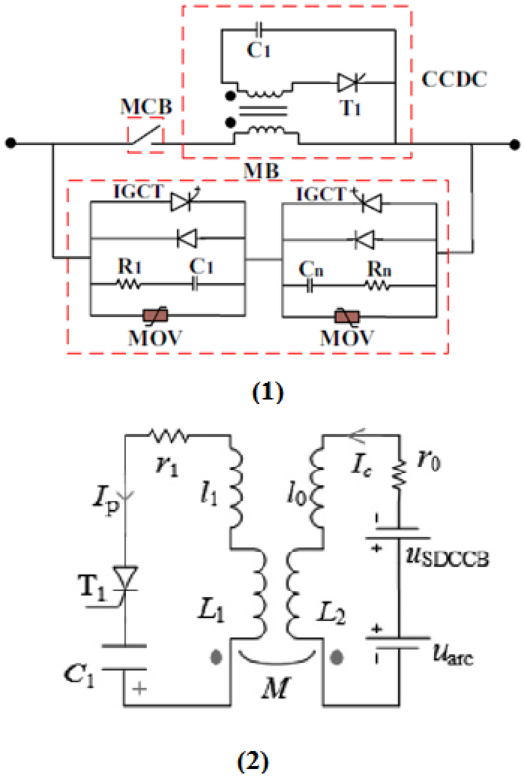

Figure 13. Structure of the CCDC Topology in a DC Circuit Breaker: (1) Circuit Schematic, (2) Equivalent Circuit of the CCDC Structure [22].

The equivalent circuit during fault operation is depicted in Figure 13(2).

Upon fault detection, an OFF signal is sent to the mechanical switch (MCB), and an ON signal is sent to the thyristor T_1. Circuit parameters are calculated using Equations (4) and (5):

$$\begin{pmatrix} L_1 + l_1 & M & 0 \\ M & -(L_2 + l_0) & 0 \\ 0 & 0 & 1 \end{pmatrix} \begin{pmatrix} \dot{i}_P \\ \dot{i}_c \\ \dot{i}_{cl} \end{pmatrix} = \begin{pmatrix} U_c - i_P r_1 \\ i_c r_0 + u_{SDCCB} - u_{arc} \\ -\frac{i_P}{C_2} \end{pmatrix} \qquad (4)$$

$$-(L_2 + l_0)\dot{i}_c = i_c r_0 + u_{SDCCB} - u_{arc} \qquad (5)$$

Here, r_1 is the resistance of the primary coil, l_1 is the stray inductance of the circuit on the primary side, r_0 is the resistance of the coil, and l_0 is the stray inductance of the circuit loop on the secondary side. u_{arc} is the MVS arc voltage, and u_{sdccb} is the SDCCB voltage drop. The state-space equations of the equivalent circuit are formulated in two phases as shown in Figure 13(2). After i_p is extinguished by T_1 at the zero-crossing point, the equations are represented as Equation 5). u_{arc} and u_{sdccb}, along with l_1, L_2, M, r_0, and r_1, are determined by the dimensions of the coupled two-coil structure. The inductances are derived by solving the static magnetic field based on the finite element method, and the resistances are obtained using Ohm's law. u_{arc} is obtained through experiments and is approximately 20 volts. The simulated circuit is implemented in the software as shown in Figure 14, with values quantitatively specified.

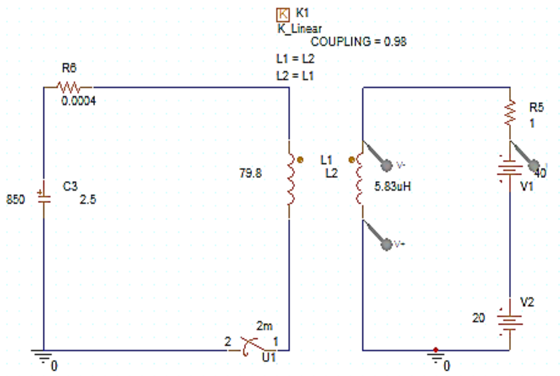

Figure 14. Equivalent CCDC circuit in PSpice

In the equivalent circuit Figure 14, for the magnetic coupling between coil L_1 and coil L_2, the K-Linear element with a maximum coupling coefficient of 98% is used in the PSpice software. Figure 15 shows the complete simulated block in the PSpice software environment.

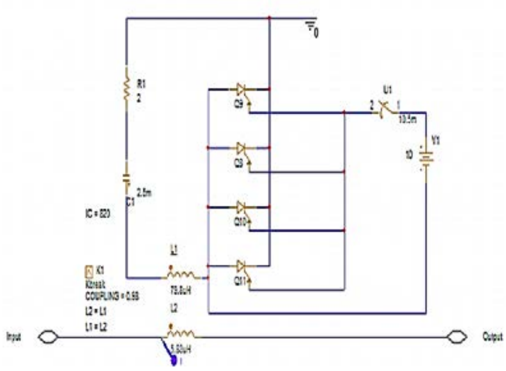

Figure 15. CCDC commutation circuit in PSpice

4.5. AC Power Supply Network

AC systems enable the application of voltages higher than 15 kV up to 25 kV, reducing line losses and increasing power at each substation, as well as providing isolation between them as a general rule. One of the disadvantages of such systems is the increased cost due to the need for insulation [26]. In this section, a sample AC network is shown in Figure 16. The performance of the HCB, when used to protect the AC feeders of railway substations, has been simulated using the PSpice software.

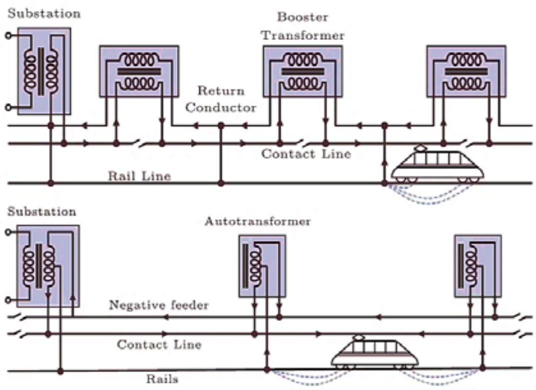

Figure 16. 25 kV AC Autotransformer and Booster Transformer Power Supply Network [26]

Table 3. AC Network Parameters

Parameter	Symbol	Value	Unit
Source Parameters			
Source Voltage	VS	24	kV-DC
Equivalent Resistance	RS	0.6	Ω
Equivalent Inductance	LS	1.2	mH
Line Parameters			
Equivalent Resistance	RL	9	Ω
Equivalent Inductance	LL	21.8	mH
Load Parameters			
Equivalent Resistance	RO	135	Ω
Equivalent Inductance	LO	0.6	H

4.6. Mechanical Switch Model

In AC railway power networks, protective switches are typically ACBs capable of interrupting short-circuit currents. The simulated AC HCB uses a mechanical switch model without the speed or actuator features of the DC counterpart. The model, shown in Figure 17, employs a vacuum chamber to manage arcing.

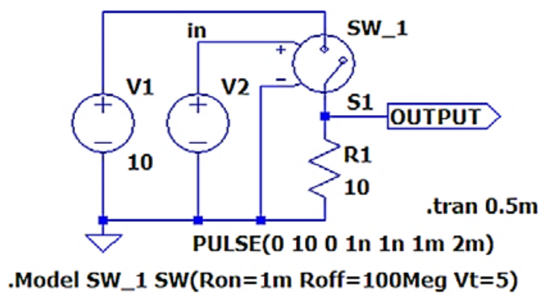

Figure 17. Proposed mechanical switch performance model in LTspice.

The zero-crossing nature of AC currents mitigates short-circuit interruption challenges, allowing MCBs to operate independently or as HCB components. These MCBs, equipped with robust arc chambers (e.g., vacuum breakers), handle arcing during commutation, falling under arc-based commutation in HCBs. In an AC power supply network with a hybrid circuit breaker, the switch model used is practically a hybrid switch model without a Thomson actuator. Thus, the switch actuator will be a vacuum chamber, as depicted in Figure 17.

4.7. Electrical Model of MOV

In the LCS topology, the MOV is omitted from the commutation branch, with a snubber circuit and MOV used together to suppress voltage transients. The MOV provides effective protection against voltage surges during faults or switching transients in an AC HCB. The MOV operating voltage is calculated based on the circuit conditions using Equation 6:

$$V_{MOV} = V_{nomial} \times \sqrt{2}(1 + \text{margin}) \quad (6)$$

In this relation, $V_{nominal}$ is the effective voltage, and the value in parentheses represents a margin of approximately 10% to 20%, which is typically added to account for transients. In a case where each switch is subjected to a nominal voltage of 25 kV, which is practically impossible, it can be expressed as Equation 7:

$$V_{MOV} = 25\text{kV} \times \sqrt{2}(1.2)\text{=42.4kV} \quad (7)$$

Under normal operating conditions and during fault conditions, a voltage of 750 V is considered for each switch. In this case, the MOV voltage will be approximately 1300 V, which ensures that the MOV clamps the voltage before it exceeds safe levels for the circuit breaker. The absorbed energy is calculated using Equation 8 where L is the circuit inductance and I_{fault} is the fault current in the solid-state switch branch.

$$E_{MOV} = \frac{1}{2} L I_{fault}^2 \quad (8)$$

4.8. LCS Topology

The LCS topology, previously applied to DC networks, is proposed for AC railway power networks (Figure 18).

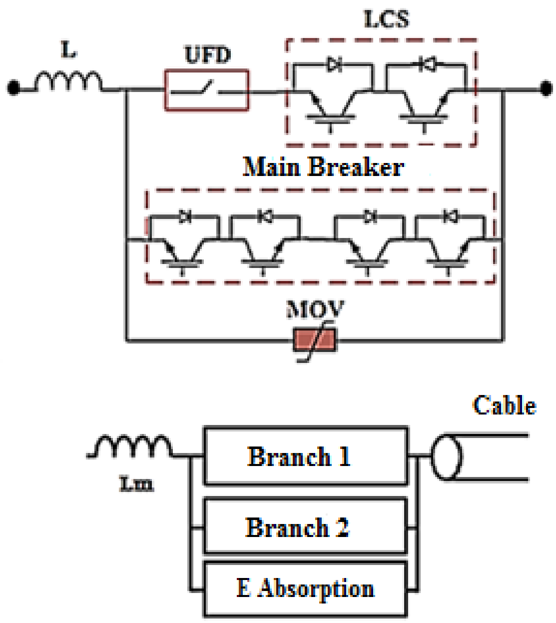

Figure 18. LCS topology structure and single-line schematic of the topology circuit [22]

For low-voltage breakers (<10 kV), the arc voltage (20 V) exceeds the solid-state switch voltage drop, enabling easy current commutation without LCS [27]. At higher voltages, the LCS ensures current commutation. An inductor in series with the hybrid circuit breaker is required to limit the rate of current rise and the maximum fault current affecting the semiconductors, thereby reducing power losses in the semiconductor branch. The inductor size is calculated using Equation 9.

$$L_m = \frac{k_{TW}.\ V_{AC}.\Delta t_{Total}}{I_{Max}} \tag{9}$$

I_{max} is the maximum breaking capacity of the main circuit breaker, Δt_{Total} is the maximum time the current is sustained in the secondary branch, and K_{TW} is a constant. K_{TW} compensates for excessive voltages across the AC-side inductance during transient faults and can typically be assumed as 1. If the circuit breaker's speed increases, it can be raised to 2, which is considered as 2 here [28]. The number of series switches required can be calculated using Equations 10 - 11.

$$n = \frac{V_{AC}\ .\ R_{var}}{(1 - S_{\mathcal{F}})V_{IGBT}} \tag{10}$$

$$R_{var} = \frac{(1 - S_{\mathcal{F}})V_{IGBT}}{(1 - S_{\mathcal{F}})V_{IGBT} - \Delta V} \tag{11}$$

The maximum voltage of each individual switch in the secondary branch is denoted, S_f is the safety margin used in the design, ΔV represents the voltage change during a transient fault in a device, and R_{var} is the ratio of the peak transient overvoltage to the AC link voltage. The equivalent circuit used at the moment of LCS turn-off is shown in Figure 19.

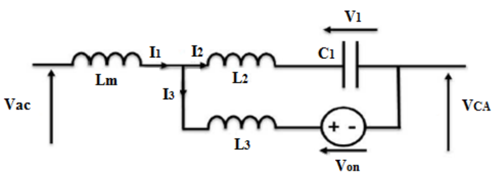

Figure 19. Equivalent LCS circuit

C_1 is the parallel capacitance around the LCS, L_2 is the inductance of the primary path, L_3 is the inductance of the secondary path, V_{on} is the on-state voltage of the secondary path, and V_{AC} is the cable voltage. In Equation 12, by formulating the state-space representation of the equivalent circuit, we obtain:

$$X = \begin{bmatrix} I_1 \\ I_2 \\ I_3 \\ V_3 \end{bmatrix}, \quad X_0 = \begin{bmatrix} I_0 \\ I_0 \\ 0 \\ V_0 \end{bmatrix}, \quad U = \begin{bmatrix} V_{AC} \\ V_{CA} \\ V_{ON} \end{bmatrix},$$

$$B = {}^{1}\!/_{(L_m L_2 + L_M L_3 + L_2 L_3)},$$

$$\begin{bmatrix} L_2 + L_3 & -(L_2 + L_3) & -L_2 \\ L_3 & -L_3 & L_m \\ L_2 & -L_2 & -(L_m + L_2) \\ 0 & 0 & 0 \end{bmatrix},$$

$$(sI - A)^{-1} = {}^{1}\!\Big/\left[\left(\frac{L_m + L_3}{C_1(L_m L_2 + L_M L_3 + L_2 L_3)}\right) + s^2\right] \tag{12}$$

The state transition matrix is provided in Equation 13.

$$\begin{bmatrix} {}^{1}\!/_{s} & \left(\frac{-L_2}{sC_1(L_m L_2 + L_M L_3 + L_2 L_3)}\right) & 0 & \left(\frac{-L_3}{(L_m L_2 + L_M L_3 + L_2 L_3)}\right) \\ 0 & s & 0 & \left(\frac{-(L_m + L_3)}{(L_m L_2 + L_M L_3 + L_2 L_3)}\right) \\ 0 & \left(\frac{L_m}{sC_1(L_m L_2 + L_M L_3 + L_2 L_3)}\right)) & {}^{1}\!/_{s} & \left(\frac{L_m}{(L_m L_2 + L_M L_3 + L_2 L_3)}\right) \\ 0 & {}^{1}\!/_{C_1} & 0 & s \end{bmatrix} \tag{13}$$

It is worth mentioning that the equivalent circuit is only valid from the moment the devices are turned off until the maximum voltage appears across the LCS. The maximum voltage across the LCS can also be estimated using Equation 14.

Knowing the maximum voltage is important for estimating losses during normal operation. The maximum voltage across the across the LCS depends on the interrupted current and the system voltage level degree, which are represented by two separate terms components in Equation 14.

$$V_1 \approx \frac{L_3(V_{AC} - V_{CA}) + L_m V_{ON}}{L_m + L_3} + I_0\sqrt{\frac{[L_2 + L_3]}{C_1}} \tag{14}$$

Since the LCS can operate within a few hundred microseconds after the moment of fault detection, the cable voltage may have a negative potential due to wave propagation effects [5]. As the cable voltage can become negative, the voltage across the LCS increases, resulting in the maximum operating voltage across the LCS occurring during a transient fault. Through analysis, the time to switch from the primary branch to the secondary branch is obtained, which is defined as the "switching time" of the circuit breaker in Equation 15.

$$t_{com} \approx \frac{1}{\omega}\left[\pi - \tan^{-1}\left(\frac{\omega I_0(L_m L_2 + L_M L_3 + L_2 L_3)}{L_3(V_{AC} + V_{CA}) + L_m V_{ON}}\right)\right],$$

$$\omega = \sqrt{\frac{L_m + L_r}{C_1(L_m L_2 + L_M L_3 + L_2 L_3)}} \tag{15}$$

4. Results and Discussions

4.1. Performance of DC Hybrid Circuit Breaker

The structure of the HCB components was analyzed, and a realistic model was simulated in PSpice and LTspice. The ideal breaker characteristic, based on [21], assumes a 12 kV breaker with a 125 A nominal current and a 0.9 ms pre-arc time, achieving a 0.5 ms interruption time in fast operation mode.

A pre-charged capacitor (950 V, 3.2 mF) is used to generate a negative voltage. Simulation results (Figure 20) show a 5 kA current in the upper branch (containing the thyristor and capacitor), with an induced voltage in L_2 (Figure 21).

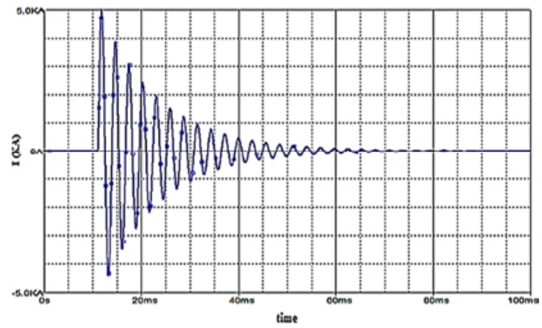

Figure 20. Current in the CCDC internal circuit

After the circuit is closed by the thyristor, the inrush current initially surges sharply to ensure the induced voltage in the secondary circuit, which is the path for the total fault current of the circuit. According to Figure 21, the voltage across L_1 is 800 V, corresponding to the changes in the passing current (phase and frequency). The coupling between the two coils is also considered to be 98%.

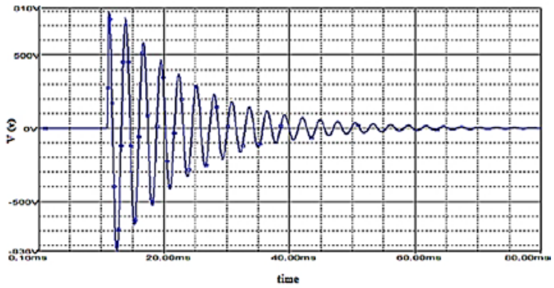

Figure 21. Induced voltage in coil L1

In the process of interrupting the fault current in the studied hybrid circuit breaker, after fault detection and the opening of the mechanical switch in the main path, as shown in Figure 22, the current at t = 10.5 ms, when the thyristor gate (a switch with synchronized closing time) is triggered, causes the CCDC circuit to induce a voltage in the main fault current path in the first branch (commutation branch). Meanwhile, after 1.5 ms, the main circuit current, following the establishment of an appropriate gap between the two contacts in the mechanical switch of the second branch, enters the solid-state switch branch at t = 10.2 ms. After an additional 0.54 ms, i.e., at t = 10.54 ms, the current becomes zero.

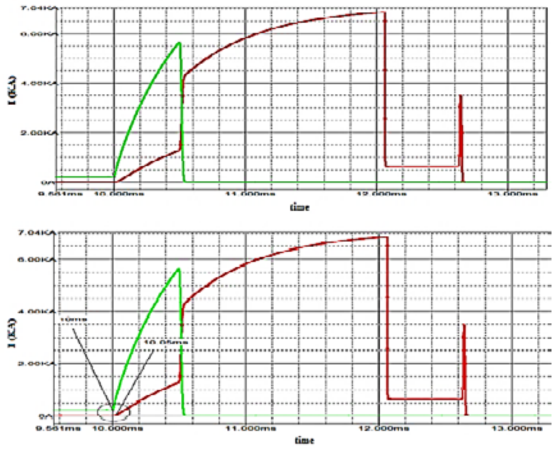

Figure 22. Current commutation in the solid-state switch branch

In the third branch, considering that the voltage across the second branch in the hybrid circuit breaker reaches approximately 7 kV from the moment of turn-on at t=12.8 ms, and briefly reaches a final value of approximately 33 kV at t=16.6 ms, with the turning off of the IGBT switches in the second branch, the short-circuit current flow in the hybrid circuit breaker causes the voltage in the third branch (MOV) to increase rapidly. This voltage rise continues up to 37 kV, or approximately 1.5 times the nominal voltage of the circuit breaker, as shown in Figure 23.

After approximately 2.8 ms, the short-circuit current is discharged, and with the current in the third branch becoming zero, the voltage across the MOV branch equals the network voltage. The entire fault current interruption process takes about 3 ms.

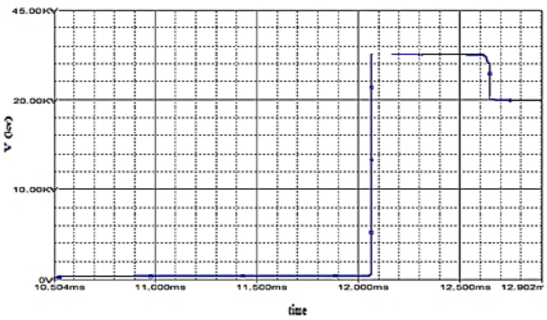

Figure 23. Voltage changes in the MOV branch

4.2. Performance of AC Hybrid Circuit Breaker

Initially, before the occurrence of a fault in the power supply system, the mentioned switch carries a current of approximately 112 A. After the onset of a short circuit at t=5 ms, the main line current and the current passing through the switch sharply increase to approximately 1080 A. In Figure 24, the voltage characteristic of the switch during interruption, which uses a vacuum as an insulator in its structure, is presented. In this figure, it is clearly visible that the voltage across the switch after the short circuit at t=5.5 ms, given that the circuit includes an LCS in its path, reaches approximately 430 kV in 0.4 ms and, after 0.17 ms, returns to the network voltage level.

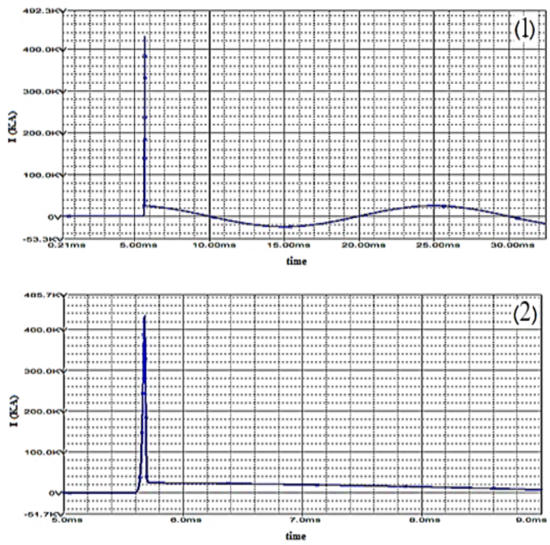

Figure 24. Mechanical switch voltage characteristics in the AC HCB

To improve the clarity of the simulation results in the AC circuit breaker section, it is advisable to present the current values on both sides of the protective breaker and the train, before and after the short-circuit event.

As shown in Figure 25, the current prior to the short circuit—under normal operating conditions in the simulation—is approximately 112 A. Considering that the short circuit occurs at t = 5 ms, the current at the moment of fault is about 100 A, which subsequently drops to zero 15 ms later, at t = 25 ms, due to the interruption in the power supply network.

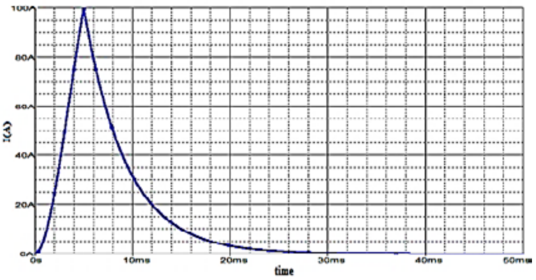

Figure 25. Current changes on the train side

Regarding the topology's operation, various scenarios can be implemented. However, to achieve the optimal interruption time and minimize stress on the switches in the AC section simulation, efforts have been made to synchronize the switching commands of the IGBTs and the topology circuit with the timing of the sensor and control signals. This approach ensures that one branch is activated (turned on) slightly before the other is deactivated (turned off). Figure 26 illustrates the current in the first branch of the hybrid AC circuit breaker, indicating that the normal supply current at the time of fault initiation t = 5 ms is about 112 A. Following the short-circuit event, the current rises sharply and reaches 840 A within 0.45 ms.

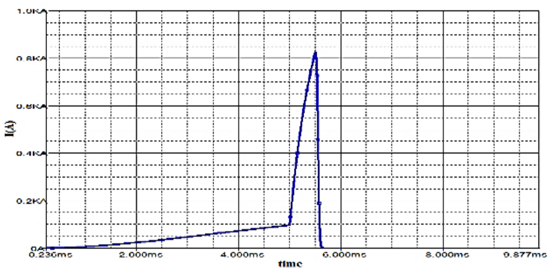

Figure 26. Short-circuit current interruption in the first branch

During the current transfer process to the second branch, according to the defined scenario, the solid-state switches in the second branch are engaged at t = 5.43 ms, receiving the turn-on signal from the control unit. As the short-circuit current enters the solid-state switch branch and begins to rise, this behavior is depicted in Figure 27. According to the Figure 27, the initiation of current flow into the second branch of the hybrid AC circuit breaker clearly illustrates the reduction in current magnitude in the solid-state switch branch. At t = 5.43 ms, the short-circuit current reaches its peak value of approximately 800 A, while at that same instant, the current in the second branch is around 27 A. Subsequently, at t = 5.6 ms, the current in the first branch (LCS circuit) drops to zero, whereas the current in the second branch (solid-state switch) continues to rise, reaching approximately 375 A. By t = 7 ms, the current in the second branch increases further to approximately 580 A.

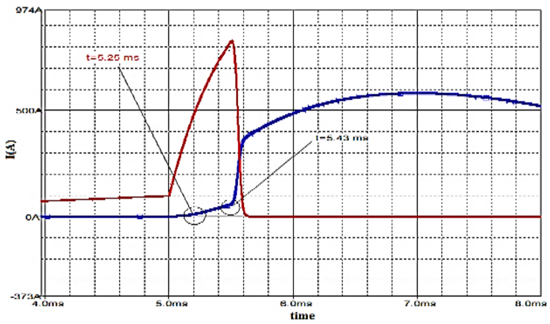

Figure 27. Short-circuit current commutation in the first and second branches

Issuing the turn-off command to the IGBT gate terminals causes the current to be interrupted within a cycle of 2ms, resulting in the main circuit current reaching zero at t = 15.5 ms. At this stage, the nominal current in the second branch falls below 150 A, and following the control signal issued by the control circuit, the current is brought to zero.

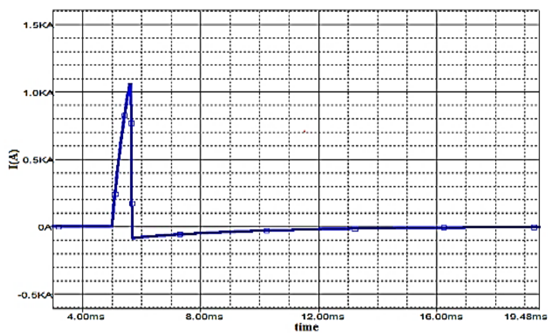

Figure 28. Short-circuit current changes on the train feeder side

As shown in Figure 28, during the interruption process in the hybrid AC circuit breaker, the short-circuit current after its initiation and rise in the power supply circuit passes through zero in both the LCS branch and the solid-state switch branch at t = 5.7 ms, over several distinct time intervals defined by the control circuit. The current then continues to decrease and reaches zero completely at t = 15.4 ms, taking approximately 10 ms. In fact, the entire interruption process spans from t = 5.5 ms to t = 15.4 ms. As evident, the fault current is brought to zero in less than 10 ms.

4. Conclusions

The results demonstrate that the hybrid DC circuit breaker offers a significantly improved interruption time approximately 2.8 ms which is nearly four times faster than that of conventional mechanical switches, indicating a clear performance advantage. In the AC section, by analyzing the LCS topology and the performance of the electromechanical switch, a substantial reduction in interruption time and up to a tenfold improvement in system response speed during short-circuit events was observed. Furthermore, the current commutation between the two branches of the breaker, along with a detailed analysis of current and voltage behavior in each section, validates the effectiveness of the proposed design. The findings of this chapter highlight the advantages of hybrid breakers over traditional systems and underscore the high potential of this technology in enhancing protection performance and safety in specialized networks such as railway power supply systems.

Declaration of Conflicting Interests

The authors declared no potential conflicts of interest with respect to the research, authorship, and/or publication of this article.

References

[1] B. Perea-Mena, J. A. Valencia-Velasquez, J. M. López-Lezama, J. B. Cano-Quintero, and N. Muñoz-Galeano, “Circuit Breakers in Low- and Medium-Voltage DC Microgrids for Protection against Short-Circuit Electrical Faults: Evolution and Future Challenges,” *Appl. Sci.*, vol. 12, no. 1, 2022, doi: 10.3390/app12010015.

[2] R. Rodrigues, Y. Du, A. Antoniazzi, and P. Cairoli, “A Review of Solid-State Circuit Breakers,” *IEEE Trans. Power Electron.*, vol. 36, no. 1, pp. 364–377, 2021, doi: 10.1109/TPEL.2020.3003358.

[3] Chen, Zhengyu and Yu, Zhanqing and Zhang, Xiangyu and Wei, Tianyu and Lyu, Gang and Qu, Lu and Huang, Yulong and Zeng, Rong, “Analysis and Experiments for IGBT, IEGT, and IGCT in Hybrid DC Circuit Breaker,” *IEEE Trans. Ind. Electron.*, vol. 65, no. 4, pp. 2883–2892, 2017, doi: 10.1109/TIE.2017.2764863.

[4] F. Ehiagwina, O. Kehinde, L. Afolabi, H. Onawola, and N. Iromini, “Applications, Prospects and Challenges of Silicon Carbide Junction Field Effect Transistor (SIC JFET),” *Int. J. Adv. Telecommun. Electrotech. Signals Syst.*, vol. 5, no. 3, pp. ۱۳۳–141, 2016. 10.1016/j.epsr.2022.107946.

[5] G. Yanxun, G. Wang, D. Zeng, H. Li, and C. Hong, “A Thyristor Full-Bridge-based DC Circuit Breaker,” *IEEE Trans. Power Electron.*, vol. PP, p. 1, 2019, doi: 10.1109/TPEL.2019.2915808.

[6] Y. He, C. Xu, Y. Li, and F. Z. Peng, “A Survey of Hybrid Circuit Breakers: Component-Level Insights to System-Wide Integration,” *IEEE Open J. Power Electron.*, vol. 5, no. March, pp. 513–533, 2024, doi: 10.1109/OJPEL.2024.3381000.

[7] V. Puumala and L. Kettunen, “Electromagnetic design of ultrafast electromechanical switches,” *IEEE Trans. Power Deliv.*, vol. 30, no. 3, pp. 1104–1109, Jun. 2015, doi: 10.1109/TPWRD.2014.2362996.

[8] C. Xu, T. Damle, and L. Graber, “A Survey on Mechanical Switches for Hybrid Circuit Breakers,” *IEEE Power Energy Soc. Gen. Meet.*, vol. 2019-August, Aug. 2019, doi: 10.1109/PESGM40551.2019.8973674.

[9] Y. Feng, X. Zhou, S. Krstic, Y. Zhou, and Z. J. Shen, “Molded Case Electronically Assisted Circuit Breaker for DC Power Distribution Systems,” *IEEE Trans. Power Electron.*, vol. 36, no. 6, pp. 6586–6595, Jun. 2021, doi: 10.1109/TPEL.2020.3037477.

[10] Xiangyu Gao, Jikun Yang, Jingen Wu, Xudong Xin, Zhanmiao Li, Xiaoting Yuan, Xinyi Shen, Shuxiang Dong, “Piezoelectric Actuators and Motors: Materials, Designs, and Applications,” *Adv. Mater. Technol.*, vol. 5, no. 1, p. 1900716, Jan. 2020, doi: 10.1002/ADMT.201900716.

[11] Yang, Q., Steurer, M., Shi, Y., Song, S., Bonaventura, N., He, Y., Hauer, J., Bosworth, M., & Graber, L. (2023). A Nonlinear Inductor-Based Fault Current Commutation Strategy to Enable Zero-Current Opening of the Mechanical Switch in a Hybrid DC Circuit Breaker. *2023 IEEE Electric Ship Technologies Symposium (ESTS)*, 498-504.

[12] D. T. Khanmiri, R. Ball, and B. Lehman, “Degradation Effects on Energy Absorption Capability and Time to Failure of Low Voltage Metal Oxide Varistors,” *IEEE Trans. Power Deliv.*, vol. 32, no. 5, pp. 2272–2280, Oct. 2017, doi: 10.1109/TPWRD.2016.2629442.

[13] S. Beheshtaein, R. M. Cuzner, M. Forouzesh, M. Savaghebi, and J. M. Guerrero, “DC Microgrid Protection: A Comprehensive Review,” *IEEE J. Emerg. Sel. Top. Power Electron.*, 2024, doi: 10.1109/JESTPE.2019.2904588.

[14] N. Doerry, “Impedance of four-conductor cable,” *Nav. Sea Syst. Command. SEA 05T Tech. Rep. Ser*, vol. 5, 2020.

[15] N. Doerry and J. V. Amy, “System Inductance for MVDC Circuit Breakers,” *2021 IEEE Electr. Sh. Technol. Symp. ESTS 2021*, Aug. 2021, doi: 10.1109/ESTS49166.2021.9512350.

[16] M. Alashi, T. Cooper, Y. Zhou, Z. J. Shen, I. Brown, and T. Wong, “Design considerations of series type hybrid circuit breaker (S-HCB),” *IET Power Electron.*, vol. 17, no. 3, pp. 364–374, 2024, doi: 10.1049/pel2.12645.

[17] P. van Gelder and J. A. Ferreira, “Zero volt switching hybrid DC circuit breakers,” *Conf. Rec. - IAS Annu. Meet. (IEEE Ind. Appl. Soc.*, vol. 5, pp. 2923–2927, 2000, doi: 10.1109/IAS.2000.882581.

[18] J. Hafner, “Proactive Hybrid HVDC Breakers-A key innovation for reliable HVDC grids,” in *Proc. CIGRE Bologna Symposium*, 2011, pp. 1–8.

[19] Zhou Jie and Li Haibin and Xie Rui and Liu Li and Nie Wenhai and Song Kun and Huo Feiyang and Liang Dapeng, “Research of DC circuit breaker applied on Zhoushan multi-terminal VSC-HVDC project,” *Asia-Pacific Power Energy Eng. Conf. APPEEC*, vol. 2016-December, pp. 1636–1640, Dec. 2016, doi: 10.1109/APPEEC.2016.7779770.

[20] A. Verdicchio, P. Ladoux, H. Caron, and C. Courtois, “New Medium-Voltage DC Railway Electrification System,” *IEEE Trans. Transp. Electrif.*, vol. 4, no. 2, pp. 591–604, 2018, doi: 10.1109/TTE.2018.2826780.

[21] T. ROBBINS, "Circuit-Breaker Model for Over-Current Protection Simulation of DC Distribution Systems," *IEEE*, 1995.

[22] Weijie Wen, Yulong Huang , Tiehan Cheng , Shutong Gao , Zhengyu Chen , Xiangyu Zhang , Zhanqing Yu , Rong Zeng , and Weidong Liu., "Research on a current commutation drive circuit for hybrid dc circuit breaker and its optimisation design," *IET Gener. Transm. Distrib.*, vol. 10, no. 13, pp. 3119–3126, Oct. 2016, doi: 10.1049/IET-GTD.2015.0840.

[23] A. B. Mirza, Y. Azadeh, H. Peng, and F. Luo, "An Isolated Voltage Injection Based Hybrid Circuit Breaker for MVDC Applications," *2021 IEEE Energy Convers. Congr. Expo. ECCE 2021 - Proc.*, pp. 608–612, 2021, doi: 10.1109/ECCE47101.2021.9595779.

[24] "Modeling of metal oxide surge arresters," *IEEE Trans. Power Deliv.*, vol. 7, no. 1, pp. 302–309, 1992, doi: 10.1109/61.108922.

[25] J. M. Meyer and A. Rufer, "A DC hybrid circuit breaker with ultra-fast contact opening and integrated gate-commutated thyristors (IGCTs)," *IEEE Trans. Power Deliv.*, vol. 21, no. 2, pp. 646–651, Apr. 2006, doi: 10.1109/TPWRD.2006.870981.

[26] P. Arboleya, C. Mayet, B. Mohamed, J. A. Aguado, and S. de la Torre, "A review of railway feeding infrastructures: Mathematical models for planning and operation," *eTransportation*, vol. 5, 2020, doi: 10.1016/j.etran.2020.100063.

[27] E. Taherzadeh, H. Radmanesh, S. Javadi, and G. B. Gharehpetian, "Circuit breakers in HVDC systems: state-of-the-art review and future trends," *Prot. Control Mod. Power Syst.*, vol. 8, no. 1, pp. 1–16, 2023, doi: 10.1186/s41601-023-00304-y.

[28] O. Cwikowski, M. Barnes, R. Shuttleworth, and B. Chang, "Analysis and simulation of the proactive hybrid circuit breaker," *Proc. Int. Conf. Power Electron. Drive Syst.*, vol. 2015-Augus, no. June, pp. 4–11, 2015, doi: 10.1109/PEDS.2015.7203574.

[29] A. Gómez-Expósito, J. M. Mauricio, and J. M. Maza-Ortega, "VSC-Based MVDC Railway Electrification System", IEEE Trans. Power Del, vol. 29, no. 1, pp. 422–430, Feb. 2014, doi: 10.1109/TPWRD.2013.2268692.

[30] T. Robbins, "Circuit-Breaker Model for Over-Current Protection Simulation of DC Distribution Systems," in *Proc. INTELEC '95 - Int. Telecommun. Energy Conf.*, Melbourne, Australia, Oct. 1995. [Available: Online].

[31] M. R. K. Rachi and I. Husain, "Metal Oxide Varistor Design Optimization and Main Breaker Branch Switch Control of a Progressively Switched Hybrid DC Circuit Breaker," in IEEE Transactions on Industry Applications, vol. 58, no. 3, pp. 3064-3075, May-June 2022, doi: 10.1109/TIA.2022.3156534.